Actuator patterns for unimorph and bimorph deformable mirrors

Sven Verpoort* and Ulrich Wittrock

Photonics Laboratory, Münster University of Applied Sciences,
Stegerwaldstrasse 39, 48565 Steinfurt, Germany

*Corresponding author: verpoort@fh-muenster.de

Received 20 January 2010; accepted 14 May 2010;
posted 20 May 2010 (Doc. ID 123024); published 22 June 2010

The actuator pattern of an adaptive mirror determines the amplitudes and the fidelities of the mirror deformations that can be achieved. In this study, we analyze and compare different electrode patterns of piezoelectric unimorph deformable mirrors using a numerical finite element model. The analysis allows us to determine the optimum actuator pattern, and it is also applicable to bimorph mirrors. The model is verified by comparing its predictions with experimental results of our prototype of a novel unimorph deformable mirror. © 2010 Optical Society of America

OCIS codes: 010.1080, 010.1285, 140.0140, 350.4600, 080.1010, 220.1080.

1. Introduction

Many applications, such as imaging and laser engineering, require the dynamic correction of wavefront aberrations that can be well characterized by Zernike modes. In the past, unimorph and bimorph piezoelectric deformable mirrors have been frequently used to compensate both dynamic and static aberrations [1–4]. Desired features of the deformable mirrors are a large stroke and a high fidelity of the mirror deformation. In many cases [5–7], the correction of aberrations with low spatial frequencies is sufficient because they usually have a higher statistical weight than the higher frequency terms. This makes unimorph and bimorph mirrors excellent candidates because they can generate low-order Zernike modes without any actuator print-through. Actuator print-through is typical of mirrors that rely on push–pull-type actuators. It leads to surface errors of high spatial frequencies, which scatter light into large angles. This is detrimental for many applications, in particular, laser resonators. Typical experimentally observed aberrations with low spatial frequencies consist of only a few low-order Zernike modes. Zernike modes represent a complete, orthonormal set of functions. Deformable mirrors can be treated as linear systems to a good approximation. We therefore analyzed and compared different unimorph mirrors with respect to the amplitude and the fidelity with which they can create certain low-order Zernike modes. For unimorph and bimorph mirrors, these amplitudes and fidelities depend critically on their actuator pattern. A variety of patterns have been used since the early days of adaptive optics [8]. However, a systematic study of the merits of the different patterns has not yet been published. In this paper, the influence of the actuator pattern on the mirror deformation is studied by analytical reasoning and by finite element modeling (FEM). The various actuator patterns are analyzed by calculating the mirror's response to the activation of each actuator. From the influence functions, we can calculate amplitudes and fidelities of arbitrary Zernike modes [9]. We found very good agreement of these calculations with the experimental results of novel unimorph mirrors that we developed.

2. Finite Element Model

FEM of complicated piezoelectric structures has already been used successfully in the past [4,10,11]. Analytical models are also described in the literature

0003-6935/10/310G37-10$15.00/0

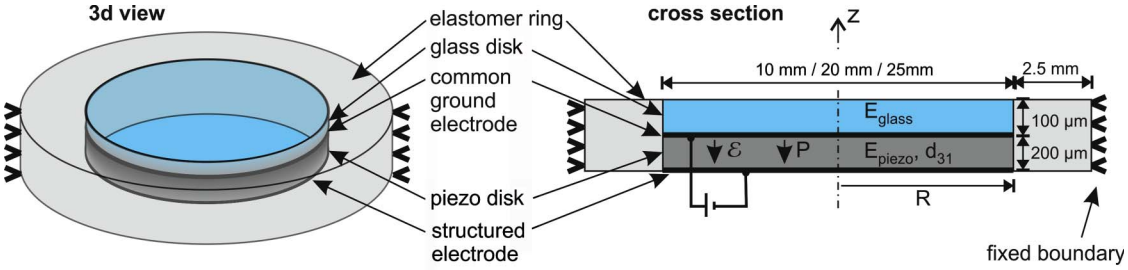

Fig. 1. (Color online) Sketch of the unimorph mirror geometry used for modeling. The sketch is not to scale: the thickness (z direction) has been magnified by almost an order of magnitude.

[12–15], but all analytical models are based on more or less severe approximations. FEM provides more precise results. For this study, unimorph mirrors consisting of a piezoelectric disk sandwiched between two metallic electrodes and bonded to a passive glass disk are modeled using the commercial FEM software package COMSOL Multiphysics 3.4. The diameter of the disks was 10, 20, or 25 mm, depending on the electrode pattern that was selected. For all the mirrors, the deformation across an optical aperture of 10 mm was calculated. This aperture is suitable for intracavity laser applications where beam diameters are small. The thickness of the piezo disk is 200 μm, and the thickness of the glass disk is 100 μm. The mirrors were assumed to be supported by a 2.5 mm wide ring of 300 μm thick elastomer. We applied fixed boundary conditions for the outer circumference of this elastomer ring. The electrode, which is situated between the glass and the piezo disk, serves as the common ground electrode for all actuators. The other electrode of the piezo disk is divided into segments that can be activated separately with different voltages. This forms the actuator pattern of the mirror. The mirror geometry, along with the boundary conditions, is shown in Fig. 1. Because the investigated electrode patterns do not have rotational symmetry, three-dimensional FEM models have been used. The hysteresis of the piezoceramic, nonlinear effects, and the influence of the bonding layer are ignored in the present study. This slightly affects the accuracy of our calculations but has no influence on the relative comparison of the electrode patterns. The validity of the FEM calculations is, however, highly dependent on the shape and the density of the numerical mesh. It is, therefore, important to optimize the mesh parameters with respect to the accuracy of the result and the computing time. In the model, a fine mesh is used in critical areas, i.e., regions where the solution gradient is high and the geometry features are small, and a coarse mesh is used in less critical areas. The mesh optimization is based on error estimates in the computed solutions and leads to an adaptively refined mesh that finally converges to approximately 250,000 nodes. The large aspect ratio, i.e., the ratio of the disks' diameters to their thicknesses, has been taken into account by a 25-times higher mesh density in the z direction, the direction of the disk's thickness. The mesh of a model built in COMSOL, as well as the calculated surface deformation under activation of a single electrode, is presented in Fig. 2. The material properties are listed in Table 1.

We compared the fidelities of the low-order Zernike modes of each mirror in open-loop control. In our approach, the shape of the deformable mirror surface is modeled as a weighted sum of the deformations $\phi_i(x,y)$ contributed by each individual actuator, where $\phi_i(x,y)$ is commonly known as the actuator influence function [3]. The surface shape $s(x,y)$ of the deformable mirror can thus be described by

$$s(x,y) = \sum_{i=1}^{n} \frac{v_i}{v_{\text{test}}} \cdot \phi_i(x,y), \tag{1}$$

where n is the number of the actuators, ϕ_i is the influence function of the ith actuator describing the surface of the mirror and has the unit μm, v_{test} is the voltage applied for determining the influence functions, and v_i is the voltage to be applied to the ith actuator. Here we use the simplification that the influence is a linear function of applied voltage. In vector form, Eq. (1) can be rewritten as

$$s(x,y) = \frac{\vec{v}_i}{v_{\text{test}}} \cdot \vec{\phi}(x,y)^T, \tag{2}$$

where $\vec{\phi}(x,y) = [\phi_1(x,y), \ldots, \phi_i(x,y), \ldots, \phi_n(x,y)]$ and $\vec{v} = [v_1, \ldots, v_i, \ldots, v_n]$. The influence function of each actuator was numerically calculated by applying a test voltage of $v_{\text{test}} = 100$ V to the actuator while setting the voltages of all other actuators to zero. Each influence function was then approximated by a 90-dimensional expansion into Zernike polynomials Z_j through a least-squares fit according to

$$\frac{\phi_i(x,y)}{v_{\text{test}}} = \sum_{j=1}^{90} \frac{a_{ij}}{v_{\text{test}}} Z_j(x,y), \tag{3}$$

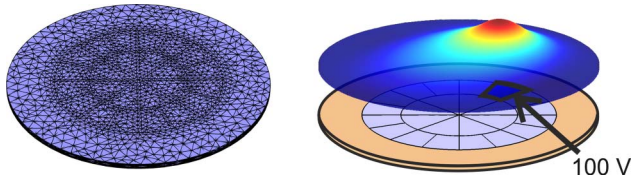

Fig. 2. (Color online) Optimized FEM mesh with 260,000 elements (left) and surface deformation of the mirror under activation of a single electrode (right).

Table 1. Material Properties and Dimensions Used in Numerical Models—Also Relevant Data for Unimorph Mirrors We Manufactured

Component	Property	Value
Piezo disk	Material	PIC255
	Disk thickness (μm)	200
	Disk diameter (mm)	10–25
	Maximum voltage (V)	$-60/+100$
	Poisson ratio v_p	0.36
	Young's modulus E_p (GPa)	62.9
	Piezoelectric strain constant $d_{31}(\mathrm{mV}^{-1})$	-174×10^{-12}
	Piezoelectricity $e(\mathrm{C\,m}^{-2})$	$e_{31}=-7.15$
	(stress-charge form)	$e_{33}=13.7$
		$e_{15}=11.90$
	Relative permittivity $\varepsilon_{\mathbf{r}}$	$\varepsilon_{T,11}=1649$
		$\varepsilon_{T,33}=1750$
	Compliance $\mathbf{S}(\mathrm{m}^2\,\mathrm{N}^{-1})$	$s_{E,11}=1.590$
		$s_{E,33}=2.097$
		$s_{E,55}=4.492$
		$s_{E,12}=-5.699$
		$s_{E,13}=-7.376$
		$s_{E,44}=4.492$
		$s_{E,66}=4.319$
Elastic support ring	Material	Polyurethane
	Width (mm)	2.5
	Thickness (μm)	~300
	Young's modulus E_e(GPa)	~0.6
Passive glass disk	Material	BK10
	Disk thickness (μm)	100
	Disk diameter (mm)	10..25
	Poisson ratio v_g	0.208
	Young's modulus E_g(GPa)	72

where $Z_j(x,y)$ are the Zernike modes (Zernike polynomials) and a_{ij} are the corresponding Zernike coefficients used to fit the influence function. Finding the best number of Zernike modes to be used for the expansion is difficult. A small number of modes leads to a less precise surface fit. On the other hand, a large number of modes can result in a higher influence of numerical errors. For our calculations, the best results have been obtained for 65 or 90 modes, so we used 90 modes in all the calculations. Again, the previous equation can be rewritten in vector form as

$$\frac{\vec{\phi}(x,y)^T}{v_{\mathrm{test}}}=\mathbf{IM}\cdot\vec{Z}(x,y)^T, \tag{4}$$

where $\vec{Z}(x,y)=[Z_1(x,y),\ldots,Z_j(x,y),\ldots,Z_{90}(x,y)]$ is the 1×90 Zernike vector and $\mathbf{IM}=[a_{ij}]/v_{\mathrm{test}}$ is the $n\times90$ influence matrix that describes the mirror. The matrix inversion of **IM** can be carried out by a singular-value decomposition (SVD) leading to the so-called control matrix $\mathbf{CM}=\mathbf{IM}^*$, the pseudoinverse of **IM**. Small singular values of the SVD-decomposed influence matrix **IM** need to be set to zero before inverting this matrix, because the corresponding modes are dominated by numerical errors.

We want to evaluate how well a mirror can generate a certain Zernike mode Z_j, which we call the "target Zernike mode." Therefore, the control matrix **CM** is used to calculate the vector of control voltages $\vec{v}$ required to produce a mirror shape that is the best fit of the desired jth Zernike mode. $\vec{v}$ is expressed in terms of the "Zernike coefficient target vector" $\vec{a}_{\mathrm{target},Z_j}$:

$$\vec{v}=\mathbf{CM}\cdot\vec{a}^T_{\mathrm{target}\,Z_j}. \tag{5}$$

The Zernike coefficient target vector has a single nonzero element if the mirror is supposed to create a pure Zernike mode. The amplitude of each Zernike coefficient target vector $\vec{a}_{\mathrm{target}\,Z_j}$ was increased until the first actuator reached the voltage limit of –60 V or +100 V. These voltage limits of –60 V and +100 V were calculated from the piezo disk thickness and the maximum allowed electric field strengths of the piezoelectric material, limited by reverse poling and electric breakthrough, respectively. A second, independent limit for the maximum amplitude of the Zernike mode was set by the fidelity of the mirror surface. We define fidelity as the inverse of the rms deviation $\sigma_{\Delta s}$ of the actual mirror surface from the target surface

$$\begin{aligned}\sigma^2{}_{\Delta s}&=\frac{1}{A}\iint_A[s_{\mathrm{actual}\,Z_j}-s_{\mathrm{target}\,Z_j}]^2\mathrm{d}x\mathrm{d}y\\&=\frac{1}{A}\iint_A\left[\sum_{j=1}^{90}(a_{\mathrm{actual}\,Z_j}-a_{\mathrm{target}\,Z_j})\cdot Z_j(x,y)\right]^2\mathrm{d}x\mathrm{d}y,\end{aligned} \tag{6}$$

where A is the area of the beam footprint. We call the area of the beam footprint on the mirror the "active area" of the mirror. It is a circle of 10 mm diameter in all mirrors we analyzed. $\sigma_{\Delta s}$ was allowed to increase up to the Maréchal criterion $\lambda/14$ [16] as the amplitude of the target Zernike mode was gradually cranked up. Therefore, the maximum Zernike amplitude that a mirror can produce can be limited by either the maximum allowed actuator voltage ("actuator saturation") or by the surface fidelity.

Our FEM analysis revealed that, for some electrode patterns, the amplitudes of several Zernike modes are limited by saturation of one or several actuators, while the surface fidelity is still much better than the Maréchal criterion. The performance of these electrode patterns might be underestimated, because leaving the saturated actuator's voltage constant while increasing all other voltages could result in a larger amplitude of the Zernike mode while still maintaining the Maréchal criterion. In order to determine the maximum amplitude within the limit of the Maréchal criterion, we used an iterative control scheme proposed by Bonora and Poletto [17]. At first, the required voltage vector $\vec{v}$ is calculated using Eq. (5). This vector is subdivided into a vector $\vec{v}'=\{v_i\in\vec{v}|v_i<v_{\max}\}$, consisting of all unsaturated actuators and a vector $v=\{v_i\in\vec{v}|v_i\geq v_{\max}\}$ consisting of the saturated actuators. The influence matrix is divided into the submatrices $\mathbf{IM}'=\{IM_i|v_i<v_{\max}\}$ and $\mathbf{IM}''=\{IM_i|v_i\geq v_{\max}\}$. Now we can calculate better voltage values $\vec{v}'$ of the unsaturated actuators, according to

$$\vec{v} = \mathbf{CM}'[\vec{a}^T{}_{\text{target}\,Z_j} - \mathbf{IM}'' \cdot \vec{v}''], \tag{7}$$

where $\mathbf{CM}'$ is the pseudoinverse of the submatrix $\mathbf{IM}'$. The new voltage vector is given by $\vec{v} = \vec{v}' \cup \vec{v}''$. This procedure is repeated iteratively until all actuators are saturated or the rms deviation $\sigma_{\Delta s}$ of the actual surface from the target surface reaches the Maréchal limit.

If a Zernike mode is identical or nearly identical to one of the mechanical eigenmodes of the mirror, the mirror is easily deformed into this Zernike mode and several actuators are saturated when the maximum amplitude of this Zernike mode is reached. In this case, the voltage range is the limiting factor and the procedure proposed by Bonora yields considerably increased amplitudes. However, a Zernike mode that has little or no similarity to one of the eigenmodes of the mirror quickly exceeds the Maréchal limit. For such a Zernike mode, which in some sense is "orthogonal" to the eigenmodes of the mirror, the optimization routine remains without effect. How close a Zernike mode is to an eigenmode or a superposition of eigenmodes of a mirror can be quantified by the so-called purity, as reported by Bonora and Poletto [17]. The purity is defined as the projection of the normalized, actual Zernike vector $\hat{\vec{a}}_{\text{actual},Z_j}$ on the target Zernike unit vector $\hat{\vec{a}}_{\text{target},Z_j}$. The normalization of these vectors is denoted by the ^ symbol:

$$p_j = \hat{\vec{a}}_{\text{target, Z}_j} \bullet \hat{\vec{a}}^T{}_{\text{actual},Z_j}. \tag{8}$$

If the mirror is able to perfectly reproduce a required Zernike mode, the purity value for this mode is 1.

Our analysis consists of five steps: (i) setup of the FEM model, (ii) calculation of the influence functions and the control matrix, (iii) calculation of the control voltages required for the generation of each target Zernike mode, (iv) evaluation of the calculated surface shapes (calculation of $\sigma_{\Delta s}$), and (v) increasing the control voltages and iteration from steps (iv) to (v).

3. Electrode Geometries

Our aim is to find the electrode pattern that can generate certain low-order Zernike terms with the highest amplitudes and the highest fidelities (i.e., the lowest rms deviation $\sigma_{\Delta s}$). Generally, the number of electrodes directly corresponds to the available degrees of freedom. Therefore, a higher number of electrodes allows us to generate higher order Zernike modes with good fidelity, so wavefront distortions with higher spatial frequency can be corrected in an adaptive optics system. However, the appropriate maximum number of electrodes is also determined by physical and technical limitations. If one applies different voltages to two adjacent electrodes, the resultant field strength in the gap between both electrodes has to stay below the depolarization field strength. This condition results in a minimum electrode spacing of approximately 150 μm for the maximum voltage of 100 V that can be safely applied to the 200 μm thick piezo disks that we used in our FEM models. Increasing the number of electrodes thus reduces the ratio of the area covered by electrodes to the total area of the mirror. This decreases the amplitude of low-order Zernike modes, for which many neighboring electrodes have similar voltages, due to the smaller effective electrode area. The dimension of each electrode should also be larger than the thickness of the piezoelectric material, so that the influence of the stray field on the adjacent electrodes remains negligible.

The mirrors we analyzed were designed for an active area of 10 mm diameter, the beam footprint. Using the previous reasoning, this results in approximately 24 electrodes under the beam footprint. Figure 3 shows the first 12 Zernike modes, with the exception of the piston term. The Zernike modes are numbered, using the single-index notation of Wyant and Creath [16]. In addition, the cumulative inflection lines of all previous Zernike modes up to the Zernike mode that is shown in false shades are shown in each graph. The last inflection line pattern can be used as a first starting point for sectioning the electrodes because inflection lines of the mirror surface can only be induced by neighboring electrodes with different signs of the applied voltage. The cumulative inflection lines of all Zernike modes up to Z_{12} in Fig. 3 would create already 48 electrodes (16 azimuthal segments times 3 radial segments). However, the middle ring is very narrow; its width is of the order of the piezo thickness. It is therefore reasonable to abandon this ring and make only one radial segmentation instead of two. We have selected the radial inflection line of Z_8, see Fig. 3, which has a radius of $r_1 = 2.7$ mm, for our active area of 10 mm diameter. This radius is found by solving

$$\frac{\partial^2 Z_8}{\partial r^2} = 0, \tag{9}$$

for a disk with simplified free boundary conditions, i.e., no circumferential stresses. The optimum radial and angular segmentation of the electrodes can be determined more precisely by the FEM simulation, taking into account the real boundary conditions. For the optimization of the radial segmentation, we have modeled a mirror without any azimuthal segmentation. The variable parameters for the optimization have been the voltages V_1 and V_2 of the two electrodes and the radius r_1 of the electrode segmentation. The optimum radius r_1 is then determined by searching for the parameter triple (V_1, V_2, r_1) corresponding to the surface shape with the least residual rms deviation $\sigma_{\Delta s}$ from the Zernike surface Z_8, which represents spherical aberration. The resultant optimum radial electrode segmentation is $r_1 = 2.85$ mm, slightly larger than our analytical result of 2.7 mm. By making just one radial segmentation, we have reduced the number of electrodes to 32, still more than 24. We further reduced the number of electrodes by dividing the circular area within r_1 into only 8 azimuthal segments of 45° each instead of the 16 azimuthal

segments shown in Z_{12} of Fig. 3. We again justify this by the fact that otherwise exceedingly small electrodes would be created. The cumulative inflection line pattern of Z_{12} in Fig. 3 would create a segmentation of the second ring into 30° and 15° segments. For comparison, we also made FEM simulations of a mirror that has 16 azimuthal segments of 22.5° each. To demonstrate the improvement in Zernike mode fidelity and amplitude due to the radius optimization, we have simulated another mirror with 22.5° segments and a nonoptimized radial segmentation at $r_1 = 3.25$ mm for comparison.

Various other electrode patterns have been used and published in the past. For example, an additional ring of electrodes could be used that is outside the active area. In the following text, we call this ring an "out-of-aperture ring." This would allow better control of the slope at the circumference of the active area. Such a design is, for example, used for bimorph mirrors manufactured by AOptix Technologies [3]. To study the influence of the width of the additional out-of-aperture ring, we simulated such electrode patterns with an outer diameter of the additional out-of-aperture electrode ring of 20 and 25 mm, while maintaining the diameter of the active area of 10 mm. In some cases, the out-of-aperture electrode ring is separated from the electrodes of the active area by an additional inactive ring called the guard ring. The purpose of the guard ring is to smooth out the transition from the out-of-aperture ring to the active area. In Ref. [18] the authors conclude that mirrors that can be described by a biharmonic equation, e.g., deformable mirrors with push–pull actuators, two out-of-aperture electrode rings are needed to generate low-order Zernike modes with high amplitude and high fidelity. Furthermore, the authors state that, for unimorph and bimorph mirrors that can be described by a Poisson equation, one out-of-aperture ring is sufficient to achieve the best amplitudes and fidelities. To verify this result, we have simulated a design with two out-of-aperture rings.

Another prominent example of electrode patterns is a honeycomb pattern of equal-area hexagonal electrodes that is frequently used for membrane mirrors. We therefore investigated honeycomb layouts with 19 and 37 electrodes.

Electrode patterns derived from Voronoi diagrams are not considered in this work. Such electrode patterns are better suited for larger mirrors with a higher number of actuators.

Figure 4 shows the 11 different electrode patterns for which we will report the results of our FEM

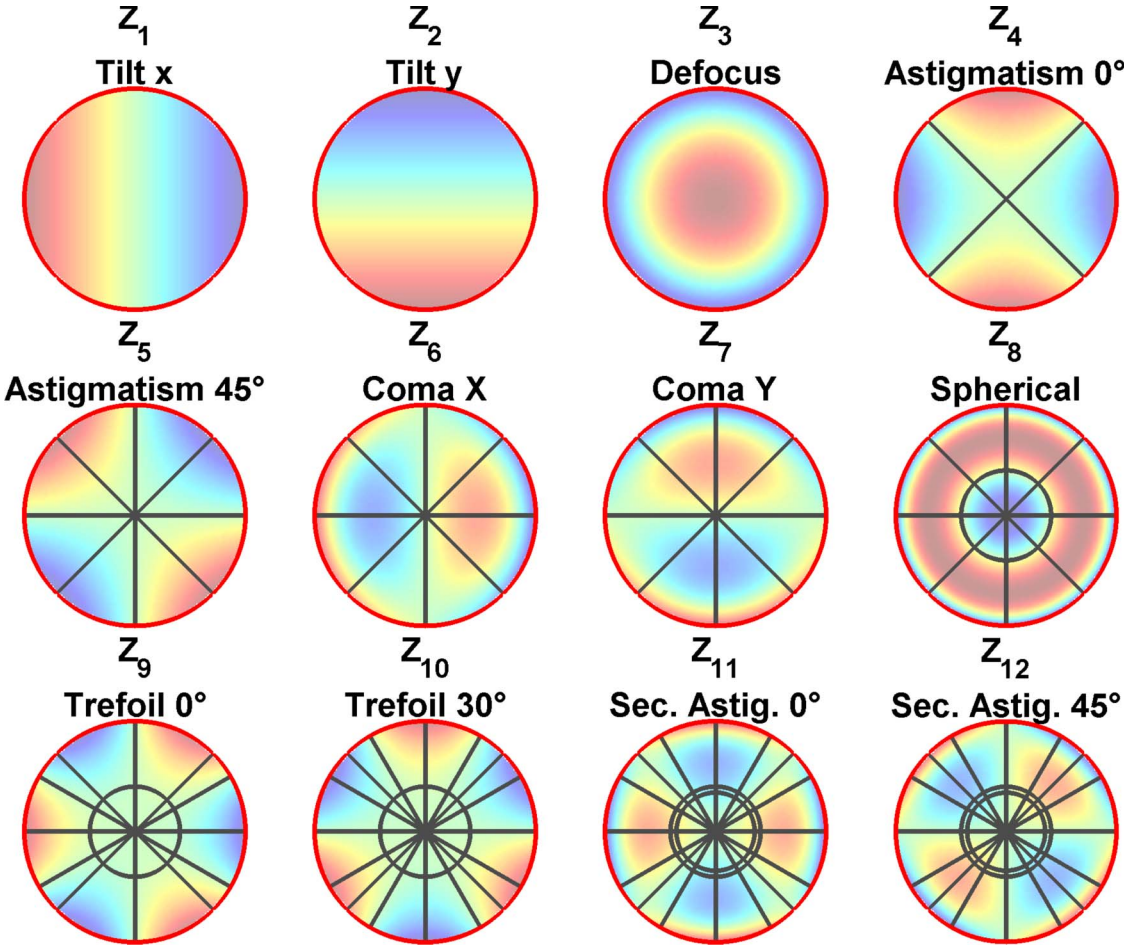

Fig. 3. (Color online) Low-order Zernike modes. The cumulated inflection lines of all previous Zernike modes up to the Zernike mode shown in false shades are indicated.

simulation in the next paragraph of this paper. The patterns can be described as follows:

a. thirty-five-actuator keystone layout with one out-of-aperture ring and a guard ring similar to the design used by AOptix,
b. forty-actuator keystone layout with one out-of-aperture ring, a guard ring, and azimuthally symmetrical electrodes,
c. fifty-six-actuator keystone layout with two out-of-aperture rings and a guard ring,
d. forty-actuator keystone layout with one out-of-aperture ring,
e. forty-actuator keystone layout with one wider out-of-aperture ring,
f. seventeen-actuator keystone layout of our unimorph prototype mirror, the contact from the ground electrode on the back side is wrapped around and visible at the six o'clock position,
g. twenty-four-actuator keystone layout with a 22.5° angular segmentation of the second ring with a first radial segmentation at $r_1 = 2.85$ mm,
h. twenty-four-actuator keystone layout with a 22.5° angular segmentation of the second ring with a first radial segmentation at $r_1 = 3.25$ mm (not optimized),
i. twenty-four-actuator keystone layout with an alternating 30° and 15° angular segmentation of the second ring,
j. nineteen hexagonal actuators arranged in a honeycomb pattern, and
k. thirty-seven hexagonal actuators arranged in a honeycomb pattern.

4. Results

In order to validate the numerical model, a prototype mirror has been constructed consisting of a 10 mm diameter, 0.2 mm thick PIC255 piezoelectric ceramic disk bonded to a 10 mm diameter, 0.1 mm thick BK10 glass substrate. The electrode is segmented into one central pad surrounded by two concentric rings with 45° subdivisions [see pattern (f) in Fig. 4]. The electrode patterning was done by laser ablation with a Q-switched Nd:YAG marking laser. To measure the influence functions of the prototype mirror, a phase-shifting interferometer has been used. The measured influence functions of the mirror were found to be in good agreement with the numerical predictions, as can be seen in Figs. 5 and 6. This is proof that our numerical FEM analysis is sufficiently accurate. As expected for a unimorph deformable mirror, the maximum amplitude of the Zernike mode is observed to be approximately proportional to the inverse square of the mode's radial order [19].

Figures 7 and 8 show the comparison of the amplitudes and purities of all 11 electrode patterns and represent the main result of this paper. The figures indicate that keystone designs with circular symmetry, such as those depicted in Figs. 4(a)–4(i), are especially suited for the generation of low-order Zernike modes. Moreover, the calculations show that electrode patterns with one out-of-aperture electrode ring can generate much larger amplitudes for some Zernike modes, as shown in Fig. 7. Only the amplitude of the defocus mode is reduced by approximately 25%. This can be explained by the fact that the best approximation of the defocus mode is achieved by applying the maximum allowed voltage to all electrodes in the active area and by applying voltages with an opposite sign to the out-of-aperture ring electrodes calculated by Eq. (5). In this way, the out-of-aperture electrodes compensate for the influence of the boundary conditions imposed by the elastomer. In case of the defocus mode, the optimization routine Eq. (7) proposed by Bonora cannot lead to an improvement because the voltages of all electrodes inside the active are already saturated and increasing the electrode voltages of the outer ring further reduces the amplitude. To further improve the achievable amplitude of the defocus mode, an evolutionary algo-

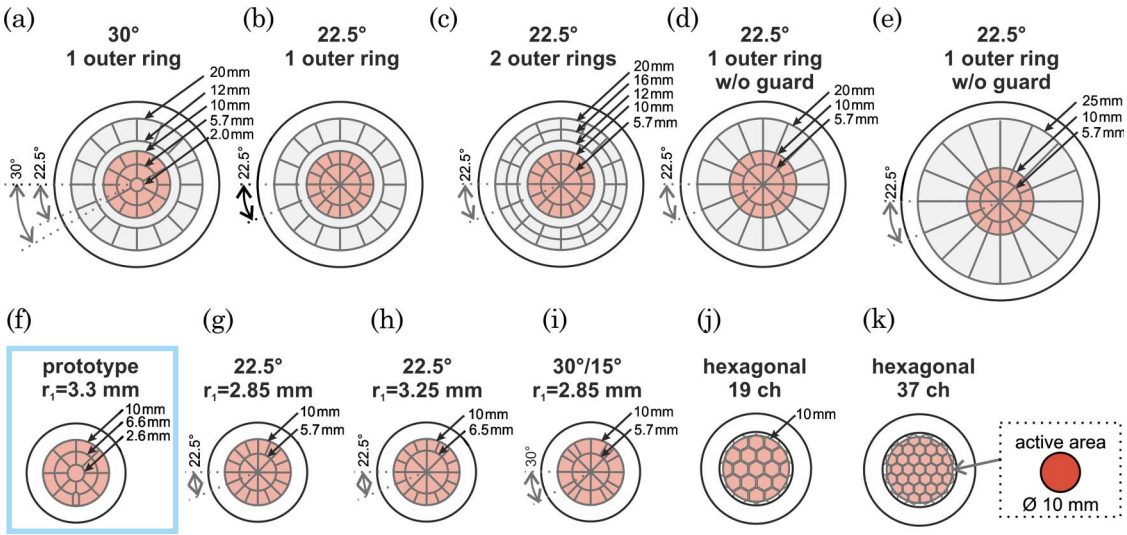

Fig. 4. (Color online) Analyzed electrode patterns. The active optical aperture is shaded red/gray.

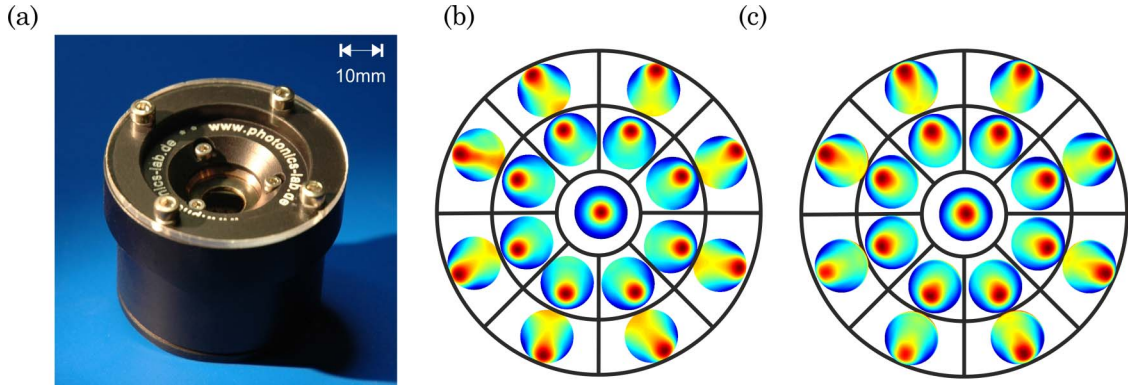

Fig. 5. (Color online) (a) Prototype mirror, (b) experimentally measured influence functions of the mirror, and (c) FEM simulation of the influence functions. Shown is the deformation generated by a single electrode activated with a voltage of 100 V. The false-shading elevation plots that represent the deformation of the whole mirror are plotted at a position that corresponds to the electrode that is being activated.

rithm could be used to determine the best voltage pattern.

The out-of-aperture electrodes also result in significantly higher purity values for all Zernike modes except for the defocus mode. An example is shown in Fig. 9. The out-of-aperture electrodes are increasing the amplitude of the astigmatism Zernike mode Z_4 from 1.1 μm to 3 μm. At the same time, fidelity is increased as well, as can be seen from the calculated interferograms in Fig. 9. This is also reflected in the purity of 1.0 for the pattern with out-of-aperture electrodes, compared to the purity of 0.94 for the same pattern without the out-of-aperture electrodes. Especially the Zernike terms Z_n^m with $n = |m|$, where Z_n^m is the double-index Zernike polynomial with the radial order n and azimuthal order $\pm m$, i.e., tip/tilt, astigmatism, and trefoil, benefit from the additional out-of-aperture electrodes. This is in good agreement with the analytical calculations presented in [18]. The comparison of the results obtained for the electrode patterns (b), (d), and (e) shows that the achievable peak-to-valley amplitudes of these Zernike modes are proportional to the out-of-aperture ring's width, whereas the influence of the out-of-aperture ring's width on the other Zernike terms remains negligible. The radial subdivision of the out-of-aperture ring into two rings does not lead to any further improvement, as can be seen by comparing the results for pattern (b) and (c). The amplitudes of the design with two out-of-aperture rings are generally slightly smaller than the amplitudes of the design with only one out-of-aperture ring. The biggest difference occurs for the spherical aberration term where the amplitude is decreased by 7%. As a result, one segmented out-of-aperture electrode ring outside is sufficient to generate low-order Zernike modes with high fidelity and high amplitude.

The optimization of the first radial segmentation improves the fidelity and amplitude of the spherical aberration and the secondary astigmatism Zernike terms Z_8, Z_{11}, and Z_{12}. This can be seen in Fig. 7, where the nonoptimized radial segmentation of the electrode pattern (h) and the prototype mirror electrode pattern (f) result in lower amplitudes compared to the optimized keystone designs (g) and (i). As stated in Section 3, the cumulative inflection line pattern suggests a segmentation of the second ring in 30° and 15° segments. However, the comparison of

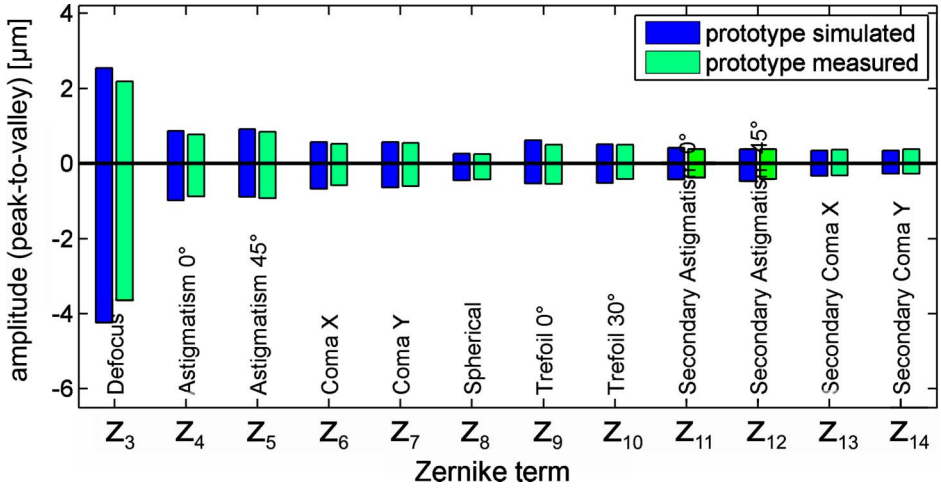

Fig. 6. (Color online) Comparison of the calculated and experimentally measured amplitudes of the prototype mirror for different Zernike modes.

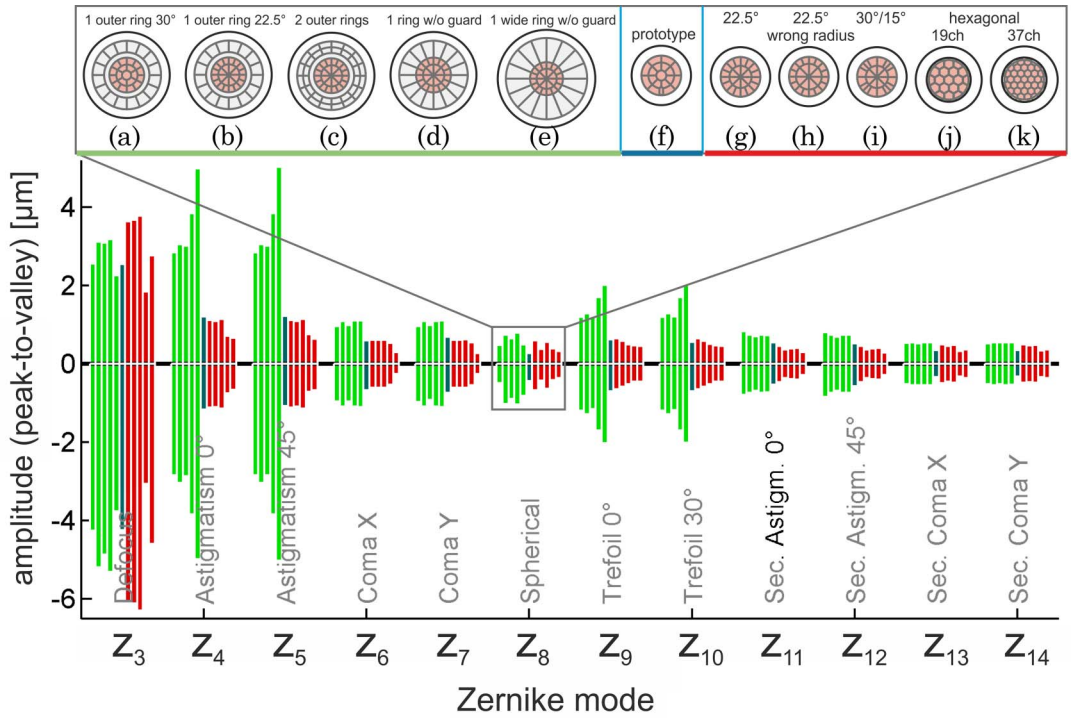

Fig. 7. (Color online) Maximum peak-to-valley Zernike amplitudes for different actuator patterns. The Zernike amplitudes are limited by the Maréchal criterion for the RMS deviation $\sigma_{\Delta s}$ or the voltage limits of the piezoceramic. The 11 bars for each Zernike mode correspond to the 11 electrode patterns shown at the top of the figure.

patterns (i) and (g) in Fig. 7 delivers nearly identical results for this pattern and the symmetrical segmentation in 22.5° sectors. The only difference is a slightly different voltage pattern. The calculations also reveal that the purity of the Zernike surfaces is almost not noticeably affected by the implementation of a guard ring, as can be seen by comparing patterns (b) and (d) in Fig. 8. Figure 7 shows that the

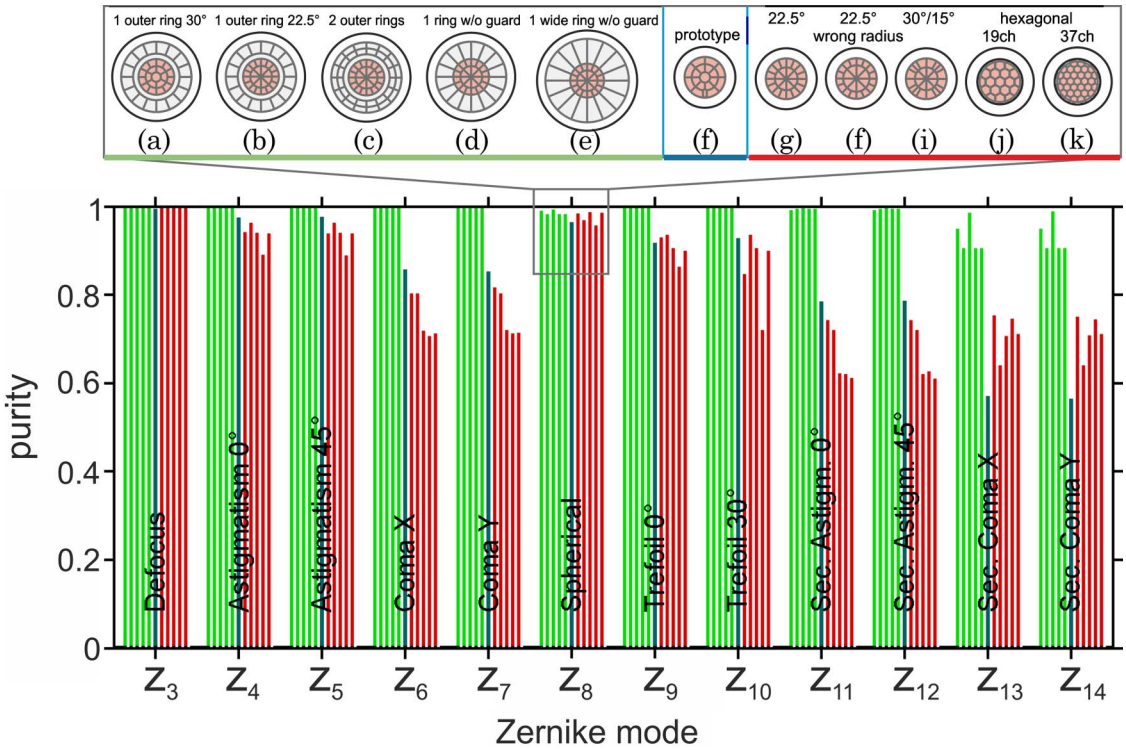

Fig. 8. (Color online) Calculated purity values for the investigated electrode patterns. The purity indicates how well the mirror can create a Zernike mode.

inactive area of the guard ring leads to significantly reduced amplitudes for some Zernike modes, e.g., Z_4, Z_5, Z_9, and Z_{10}. Besides the results given in this study, the simulations have shown that relaxing the rms deviation $\sigma_{\Delta s}$ of the target surface beyond the Maréchal limit of $\lambda/14$ results in smaller differences between the electrode patterns with and without an additional out-of-aperture ring. This is explained by the fact that mirror designs with an out-of-aperture ring are mainly limited by actuator saturation, whereas designs without an out-of-aperture ring are mainly restricted by the limit of the rms-deviation $\sigma_{\Delta s}$. Accordingly, the use of piezoelectric materials with higher depolarization field strengths (corresponding to higher voltage limits) would result in higher amplitudes for the most Zernike modes if an out-of-aperture ring of electrodes is employed. How important it is to optimize the electrode pattern can be seen, for example, by comparing the amplitudes of the astigmatism Zernike modes Z_4 and Z_5 for the hexagonal pattern (k) and the keystone pattern (e). The amplitude of the hexagonal pattern of $0.69\,\mu$m is only 13% of the amplitude achieved by the keystone layout with one outer ring, which is $4.99\,\mu$m.

5. Discussion and Conclusion

We have presented a procedure that leads to optimum actuator patterns for unimorph or bimorph mirrors. Analytical reasoning regarding the inflection lines of Zernike modes and the maximum number of electrodes was used to establish a starting pattern. This pattern was then optimized using extensive, experimentally validated, FEM computations with high spatial resolution. We computed and compared 11 different actuator patterns. About 500 hours of CPU computing time on a fast PC was required for the FEM computations of this study.

Obviously, deformable mirrors for different tasks will have different optimum actuator patterns. We searched specifically for the optimum actuator pattern for a unimorph mirror of 10 mm active area, 0.3 mm thickness, and Zernike modes up to Z_{14} (secondary coma). We found that our pattern (e) achieves the highest amplitudes for all Zernike modes except for the defocus mode. For this mode, patterns (g) to (i) achieve about 25% more stroke, but for all other modes, these patterns are much worse than pattern (e).

Even though our numerical FEM computations had to be performed for specific mirror dimensions and for a specific set of Zernike modes, we can draw some general conclusions. One ring of actuators that is outside the beam footprint on the mirror increases the amplitude of all Zernike modes with an azimuthal order identical to that of the radial order. This outer ring of electrodes has no drawbacks for the other Zernike modes, only the defocus mode suffers slightly. Honeycomb patterns of hexagonal actuators, which have been widely used for micromachined membrane mirrors, are not very suitable for unimorph and bimorph mirrors.

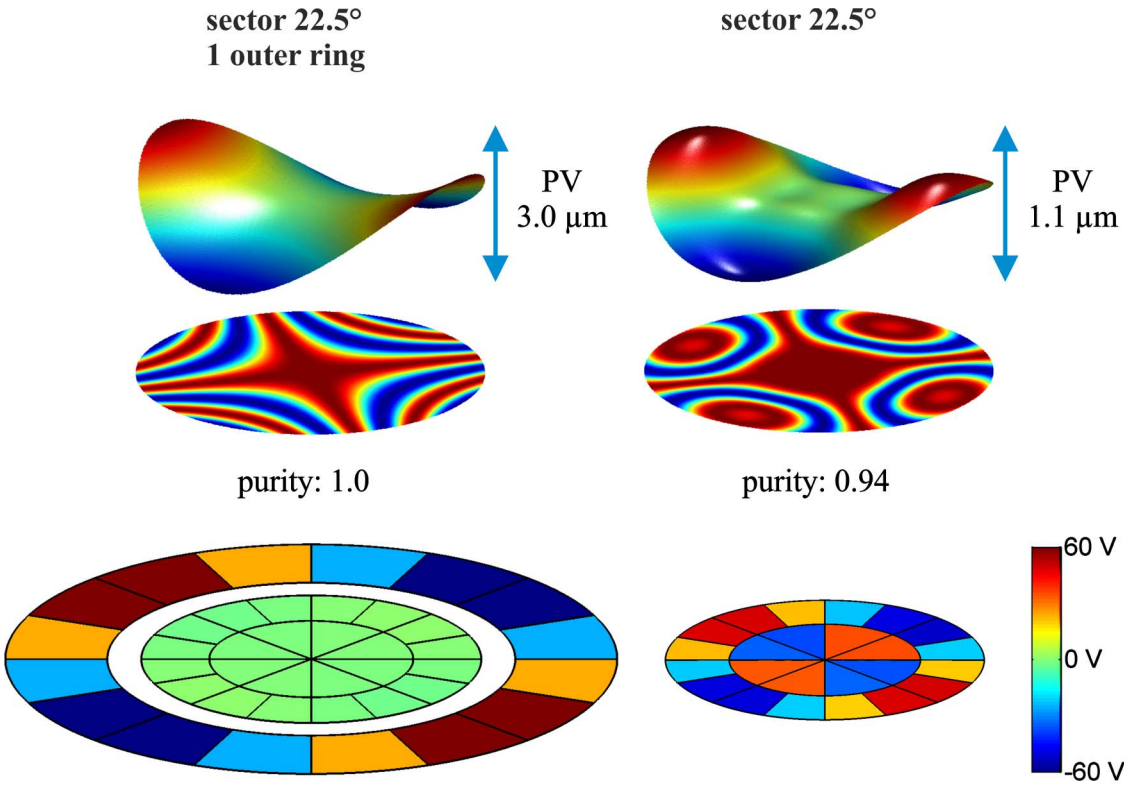

Fig. 9. (Color online) Astigmatism Zernike amplitudes and purities of the 22.5° electrode pattern with and without an additional outer ring outside of the active optical area. The surface deformation, the corresponding interferogram, and the applied voltages are plotted from top to bottom.

The general procedure we have outlined for determining the optimum actuator pattern can readily be applied to any deformable mirror. Input data for the procedure are the mirror geometry and the required amplitudes of the Zernike modes, which have to be derived from the application.

The authors gratefully acknowledge support for the work presented by the German Ministry for Education and Research under contract 1726X09 and by Thorlabs GmbH.

References

1. E. Steinhaus and S. G. Lipson," Bimorph adaptive mirrors and curvature sensing," J. Opt. Soc. Am. **69**, 478–481 (1979).
2. J. Paufique, P. Biereichel, R. Donaldson, B. Delabre, E. Fedrigo, F. Franza, P. Gigan, D. Gojak, N. Hubin, M. Kasper, U. Käufl, J.-L. Lizon, S. Oberti, J.-F. Pirard, E. Pozna, J. Santos, and S. Stroebele, "MACAO-CRIRES: a step towards high resolution in infrared," Proc. SPIE **5490**, 216–227 (2004).
3. D. A. Horsley, H. K. Park, S. P. Laut, and J. S. Werner, "Characterization for vision science applications of a bimorph deformable mirror using phase-shifting interferometry," Proc. SPIE **5688**, 133–144 (2005).
4. C. S. Long, P. W. Loveday, and A. Forbes, "Development of a piezoelectric adaptive mirror for laser beam control," in *Proceedings of ACTUATOR 2008, 11th International Conference on New Actuators* (HVG Hanseatische Veranstaltungs GmbH, 2008), pp. 584–587.
5. P. Welp, H.-M. Heuck, and U. Wittrock, "Intracavity adaptive optics optimization of an end-pumped Nd:YVO_4 laser," in *Proceedings of the 6th International Workshop on Adaptive Optics for Industry and Medicine*, C. Dainty, ed. (Imperial College Press 2008), pp. 413–418.
6. J. Graves, M. Northcott, F. Roddier, C. Roddier, D. Potter, D. O'Connor, F. Rigaut, and M. Chun, "First light for Hokupa'a 36 on Gemini North," Proc. SPIE **4007**, 26–30 (2000).
7. J. Porter, A. Guirao, I. Cox, and D. Williams, "Monochromatic aberrations of the human eye in a large population," J. Opt. Soc. Am. A **18**, 1793–1803 (2001).
8. E. Dalimier and C. Dainty, "Comparative analysis of deformable mirrors for ocular adaptive optics," Opt. Express **13**, 4275–4285 (2005).
9. E. J. Fernández and P. Artal, "Membrane deformable mirror for adaptive optics: performance limits in visual optics," Opt. Express **11**, 1056–1069 (2003).
10. G. Rodrigues, R. Bastaits, S. Roose, Y. Stockman, S. Gebhardt, A. Schönecker, P. Villon, and A. Preumont, "Modular bimorph mirrors for adaptive optics," Opt. Eng. **48**, 034001 (2009).
11. V. Piefort, "Finite element modeling of piezoelectric active structures," Ph.D. dissertation (Université Libre de Bruxelles, 2001).
12. E. M. Ellis, "Low-cost bimorph mirrors in adaptive optics," Ph.D. dissertation (Imperial College of Science, Technology and Medicine—University of London, 1999).
13. Y. Ning, W. Jiang, N. Ling, and C. Rao, "Response function calculation and sensitivity comparison analysis of various bimorph deformable mirrors," Opt. Express **15**, 12030–12038 (2007).
14. C. Schwartz, E. Ribak, and S. G. Lipson, "Bimorph adaptive mirrors and curvature sensing," J. Opt. Soc. Am. A **11**, 895–902 (1994).
15. A. Kudryashov and V. Shmalhausen, "Semipassive bimorph flexible mirrors for atmospheric adaptive optics applications," Opt. Eng. **35**, 3064–3073 (1996).
16. J. C. Wyant and K. Creath, "Basic wavefront aberration theory for optical metrology," in *Applied Optics and Optical Engineering*, R. R. Shannon and J. C. Wyant, eds. (1992), pp. 1–53.
17. S. Bonora and L. Poletto, "Push-pull membrane mirrors for adaptive optics," Opt. Express **14**, 11935–11944 (2006).
18. G. Vdovin, O. Soloviev, A. Samokhin, and M. Loktev," Correction of low order aberrations using continuous deformable mirrors," Opt. Express **16**, 2859–2866 (2008).
19. F. Roddier, "Adaptive optics in astronomy," 1st ed. (Cambridge U. Press, 1999).